LANGMUIR

Molecular Dynamics Study of Binary Nanodroplet Evaporation on a Heated Homogeneous Substrate

Jia-Jian Zhang, Haibo Huang,* and Xi-Yun Lu

Read Online

ACCESS | Metrics & More | Article Recommendations

ABSTRACT: The evaporation mechanism of miscible binary nano-droplets from heated homogeneous surfaces was studied by molecular dynamics simulations, which has never been studied before. The binary droplets contain a hydrophilic component (type-2 particles) and a hydrophobic component (type-3 particles). It is shown that liquid−liquid interaction strength (ε_{23}) and hydrophilic particle number fraction (φ) have great influence on the surface tension, wetting characteristics, evaporation patterns, evaporation rate, and local mass flux. It is observed that when $\varepsilon_{23} \geq 1$, or $\varphi \approx 0.5$, the evaporation mode is the constant-contact-angle mode. Otherwise, it is the mixed mode. We found that the evaporation rate becomes faster when φ and ε_{23} increase. The droplets become more hydrophilic when φ increases, which promotes heat transfer efficiency between the liquid−solid interface. Besides, a larger ε_{23} promotes the heat transfer inside the droplet. The mass transfer to the vapor phase occurs preferentially in the vicinity of TPCL (three phase contact line) in the hydrophilic systems ($\theta < \theta_c$), where θ_c is the critical contact angle, while in most hydrophobic systems ($\theta > \theta_c$), the mass flux close to the TPCL is suppressed. We found that $\theta_c \in (102°−106°)$, which is different from the theoretical one, $\theta_c = 90°$. The discrepancy is attributed to the existence of the adsorption layer near the TPCL.
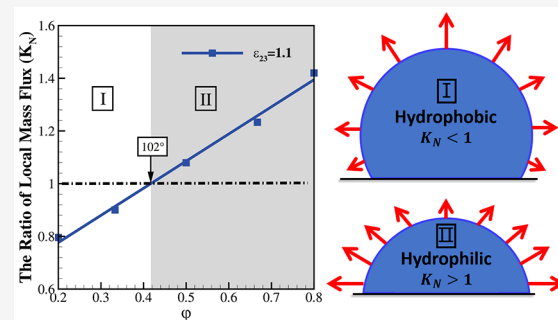
INTRODUCTION

Sessile droplets evaporation is a common natural phenomenon, and it has aroused significant interest in the latest decades because of its varied applications in technology and biology, such as inkjet printing,[1,2] DNA stretching and DNA mapping,[3,4] coating,[5] and nanopatterning.[6] A thorough understanding of this ubiquitous process is helpful to design functional patterns and produce smart devices. A significant amount of experimental and theoretical work has been carried out to understand the behavior or mechanism of pure droplet evaporation. Some studies focused on how the contact line and contact angle change during evaporation, while some highlighted factors influencing the evaporation rate.[7−21] The first theory of the evaporation of a free droplet surrounded by gas was proposed by Maxwell about 100 years ago.[22] Since then, relevant theories have been further developed and refined. For instance, based on the dynamics of the contact line and contact angle, three different evaporation modes have been proposed: the constant contact radius (CCR) mode,[7,12,19,23] the constant contact angle (CCA) mode,[10,12,16,19] and the mixed mode.[12,19] In the CCR mode, the contact line is pinned and immobilized on the solid substrate and contact area remains constant, which result in a diminishing contact angle during evaporation. In the CCA mode, the contact line keeps on receding toward the center of the droplet while the contact angle remains unchanged. In the mixed mode, both the contact line length

and contact angle change during evaporation, which usually takes place at the end of evaporation.

Although the evaporation of droplets consisting of a pure liquid has been extensively studied, there are few studies on the evaporation of multicomponent droplets. The evaporation shows a far more complex evolution due to the coupling of multicomponent evaporation, flow, and heat transfer of the mixture. Multicomponent droplets evaporation is very important in many applications such as hydrocarbon fuel evaporation in the internal combustion engine,[24] inkjet printing,[1,2] cosmetics,[25] organization of nanostructures by evaporation-induced self-assembly[26,27] and the suppression of the coffee-ring effect.[28,29]

A series of experimental studies have been carried out to investigate the binary droplets evaporation on various substrates.[29−43] In particular, evaporation of binary ethanol−water solution droplets is important because ethanol is widely used.[29,41] Besides, ethylene glycol[32] or methanol[34]/water
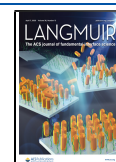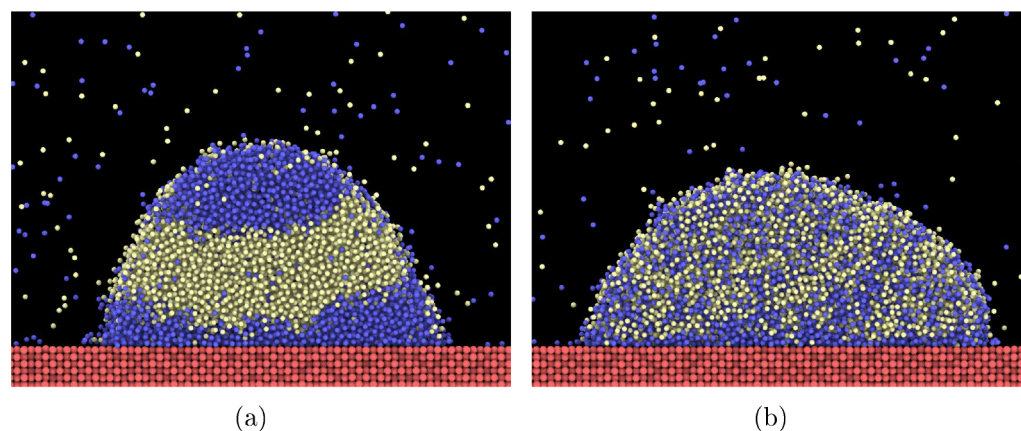
Figure 1. Schematic diagram for a binary cylindrical droplet on a homogeneous substrate when $\varphi = 0.5$, $T = 0.67$. (a) $\varepsilon_{23} = 0.8$, (b) $\varepsilon_{23} = 0.9$. The red (type-1), blue (type-2), and yellow (type-3) particles represent the solid wall, hydrophilic particles, and hydrophobic particles, respectively. The thermostat was applied to the substrate atoms to mimic the heating process.

droplets also have been experimentally studies because these organic solvents are highly volatile and similar to ethanol/water droplets. For example, Sefiane et al.[30] studied evaporation of water−ethanol binary droplets with a volume of 0.5 μL on a rough polytetrafluoroethylene (PTFE) substrate under controlled pressure at ambient temperature. They found that there are three different stages based on the evaporation rate, and the change of contact angle is nonmonotonic. In the first stage, the contact angle decreased due to the pinning of the drop on the rough PTFE surface. However, in the second stage, contact angles increased because the ethanol concentration decreases through the vaporization of the more volatile component. In the third stage, with less volatile component, the droplet almost consisted of pure water. The evaporation was similar to that of a water droplet; i.e., height and base width of the droplet decreased until it disappeared. Cheng et al.[33] studied the drop evaporation of ethanol−water mixtures having a volume of 2.0 μL at different concentrations on very flat gold surfaces. In their study, a preliminary increase in contact angle along with a sharp decrease in contact area was initially observed. Then the contact angle became constant and the contact area decreased slowly and linearly. In the above two studies, the contact angles variation at the beginning was different. Cheng et al.[33] attributed the difference to the roughness property of the surfaces.

From the numerical point of view, the evaporation of a sessile multicomponent droplet constitutes a challenging problem, since multifarious coupled effects have to be taken into account, such as the vapor−liquid equilibrium of each component, the latent heat of evaporation. Recently, a model for sessile multicomponent droplets has been developed and successfully validated based on experimental data for water−ethanol droplets.[44] The model was also able to predict the onset of oil-nucleation and the volume evolution of the ouzo droplet.[45] However, the model is limited to small contact angles because it is based on lubrication theory. Furthermore, thermal convection has been neglected. To overcome these limitations, a novel numerical model is proposed by Diddens.[46] In the model, the finite element method without invoking the lubrication approximation of the Navier−Stokes equation is used.

A series of MD simulations have been performed to examine the pure nanodroplet evaporation on various substrates.[47−54] We would like to introduce them briefly in the following. First,

the evaporation of pure nanodroplets on chemically stripe-patterned surfaces under a constant-temperature condition was carried out by Wang and Wu.[47] Second, Zhang et al.[48] proposed a nanoscale explanation for pinning during evaporation; i.e., the pinning should be interpreted as a drastic slowdown of the contact line dynamics during the transition between two contact angle boundaries. Zhang et al.[49] also studied the time evolution of nanodroplets shapes and the evaporation rate of pure nanodroplets on heated homogeneous substrates. Third, Wan et al.[50] simulated the evaporation of nanoscale droplets on hydrophobic−hydrophilic patterned surfaces, and they found that the evaporation is unexpectedly faster than that on any surfaces with uniform wettability. Wan et al.[51] also studied the evaporation of a tiny amount of water on the solid surface with different wettabilities. Fourth, Xie et al.[52] investigated the flux distribution of evaporating pure nanodroplets under three different evaporation modes. Yu et al.[53] studied the energy transport mechanism through the solid−liquid interface for the evaporating process of an argon droplet on heated substrates. Finally, Zhang et al.[54] studied the relationship between the moving speed of contact line and the intrinsic energy barrier, evaporation rate by simulating the evaporation of pure nanodroplets on heated heterogeneous surfaces. All of these works studied the evaporation of pure nanodroplets on various substrates. There are few studies on the evaporation of multicomponent nanodroplets.

This paper presented a series of MD simulations of the evaporation process of binary nanodroplets on heated homogeneous substrates. For convenience, a cylindrical binary nanodroplet was used in our simulations. To the best of our knowledge, this is the first MD study about binary droplet evaporation on heated homogeneous substrates. In Numerical Methods, the details about the model and methods used in our simulations are presented. In Results and Discussion, the wetting properties, surface tension, evaporation patterns, binary droplet size, and local mass flux will be discussed. Finally, in Summary and Conclusions, the concluding remarks are presented.

■ NUMERICAL METHODS

The simulation set up for evaporation of a binary nanometer-sized cylindrical droplet on a heated homogeneous substrate is shown in Figure 1. There are three phases in the systems, i.e., the liquid phase, the vapor phase, and the solid substrate. The solid substrate is

composed by the red particles that is named type 1, while the liquid and vapor phases are composed by the blue hydrophilic and yellow hydrophobic particles, respectively. They are named type-2 and type-3, respectively. Lennard−Jones atoms with the parameters of argon were used to model the fluid−vapor phase, because this atomic fluid has been extensively studied both experimentally and theoretically. To simplify the system, Lennard−Jones atoms were employed to model the solid substrate. The total number of argon atoms for the liquid and gas phases was 11 700. Initially these atoms were distributed on a cubic lattice with a density close to the liquid density. The solid substrate was modeled as an fcc lattice containing six layers with 1064 atoms each. The solid substrate was placed at the bottom of the computational domain under the cubic lattice containing the liquid atoms.

The interaction between the atoms in the systems is described by a 12−6 Lennard−Jones potential ($U(r_{ij})$):

$$U(r_{ij}) = 4\varepsilon_{ij}\left[\left(\frac{\sigma_{ij}}{r_{ij}}\right)^{12} - \left(\frac{\sigma_{ij}}{r_{ij}}\right)^{6}\right] \tag{1}$$

where ε_{ij} is the interaction strength between particles of types i and j, σ_{ij} is the characteristic size of the particles, and r_{ij} is the distance between the two particles. The interaction parameters between type-2 and type-2 were $\sigma_{22}^{*} = 0.3405$ nm and $\varepsilon_{22}^{*} = 0.992$ kJ/mol. The mass of the type-2 particles was $m_{2}^{*} = 6.63 \times 10^{-26}$ kg. The mass of type-3 particles was identical to that of type-2 particles, while the solid atoms were 10 times heavier than type-2. The characteristic temperature of the liquid and vapor was $T^{*} = 119.8$ K, and its normalized value was $T = k_{B}T^{*}/\varepsilon_{22}^{*} = 1$. The time unit was $\tau = (m_{2}^{*}\sigma_{22}^{*2}/\varepsilon_{22}^{*})^{1/2}$. In our simulation, the other parameters which are normalized by the corresponding parameters of type-2 particles are shown in Table 1. It

Table 1. Dimensionless Parameters Used in the MD Simulations

$i-j$	ε_{ij}	σ_{ij}
1−1	10.0	1.2
1−2	0.7	1.1
1−3	0.4	1.1
2−2	1.0	1.0
2−3	0.9−1.1	1.0
3−3	1.0	1.0

is seen from Table 1 that two different liquid−solid strengths were used. From our results, the equilibrium contact angles for $\varepsilon_{13} = 0.4$ and $\varepsilon_{12} = 0.7$ are 119° (hydrophobic) and 79° (hydrophilic), respectively, at $T = 0.67$.

The simulations were performed in an NVT ensemble, where the Berendsen thermostat was chosen to control the temperature with a coupling time of 0.25τ. Note that the thermostat was only applied to the substrate atoms to mimic the heating process. The dimensions of the computational domain in the x, y, and z directions were $144.4\sigma_{22}$, $13.3\sigma_{22}$, and $274.2\sigma_{22}$, respectively, where z was the surface normal. Periodic boundary conditions in the three directions of space were applied in all simulations. The simulations were carried out using LAMMPS.[55] The time step and the cutoff were set to be 0.0025τ and $4.4\sigma_{22}$, respectively.

Initially, there was no gas phase in the computational domain and all fluid particles were placed on a cubic lattice with a density close to the liquid density. At beginning, the temperature of the whole system, including the substrate, was $T = 0.67$. The system relaxed to its equilibrium state where a droplet surrounded by a vapor phase was formed and the temperature everywhere was the initial T. Furthermore, at the equilibrium state, the droplet size did not change any longer. The relaxation stage typically took about $25\,000\tau$. After the system reached the equilibrium state, the droplet was heated by suddenly increasing the temperature of the substrate to $T = 0.83$, yielding droplet evaporation. And during this process, at least 15 million time steps ($37\,500\tau$) were performed to collect enough data for further analysis of the evaporation properties. The size of the droplet and its variation upon evaporation were obtained by means of a cluster analysis. Two atoms were considered to be part of the same cluster if the distance between them was smaller than $1.5\sigma_{22}$.

In our study, we focused on two factors affecting droplet evaporation: the interaction strength (ε_{23}) between binary droplets and the mass fraction of each component. Because the mass of a type-2 particle is identical to that of a type-3 particle, the mass fraction is equal to the number fraction of particles. The parameter φ was used to quantify the number fraction of the hydrophilic particles (type-2) in the total liquid−vapor phase. Five typical φ were chosen in our study, i.e., $\varphi = 0.2, 0.33, 0.5, 0.67, 0.8$.

The interaction strength ε_{23} would significantly affect the mixing degree of binary droplets. The instantaneous shapes of the binary droplets with $\varepsilon_{23} = 0.8, 0.9$ are shown in Figure 1(a) and Figure 1(b), respectively, when the system temperature is $T = 0.67$ and $\varphi = 0.5$. From Figure 1(a), we can see that when $\varepsilon_{23} = 0.8$, inside the droplet the two components are stratified; i.e., the mixing degree between them is low. However, when $\varepsilon_{23} = 0.9$, the mixing degree is high
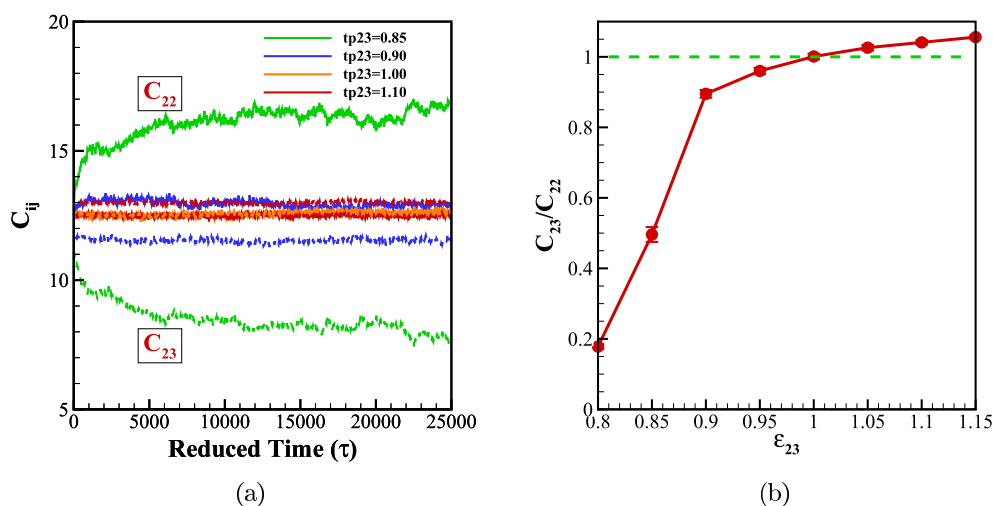

Figure 2. (a) Coordination number C_{ij} as a function of time for different ε_{23}. The solid line and the dashed line denote C_{22} and C_{23}, respectively. (b) The rate between C_{23} and C_{22} for various interaction strength ε_{23} and the green long-dashed line denotes $C_{23}/C_{22} = 1.0$. Here in all cases $\varphi = 0.5$ and $T = 0.67$.
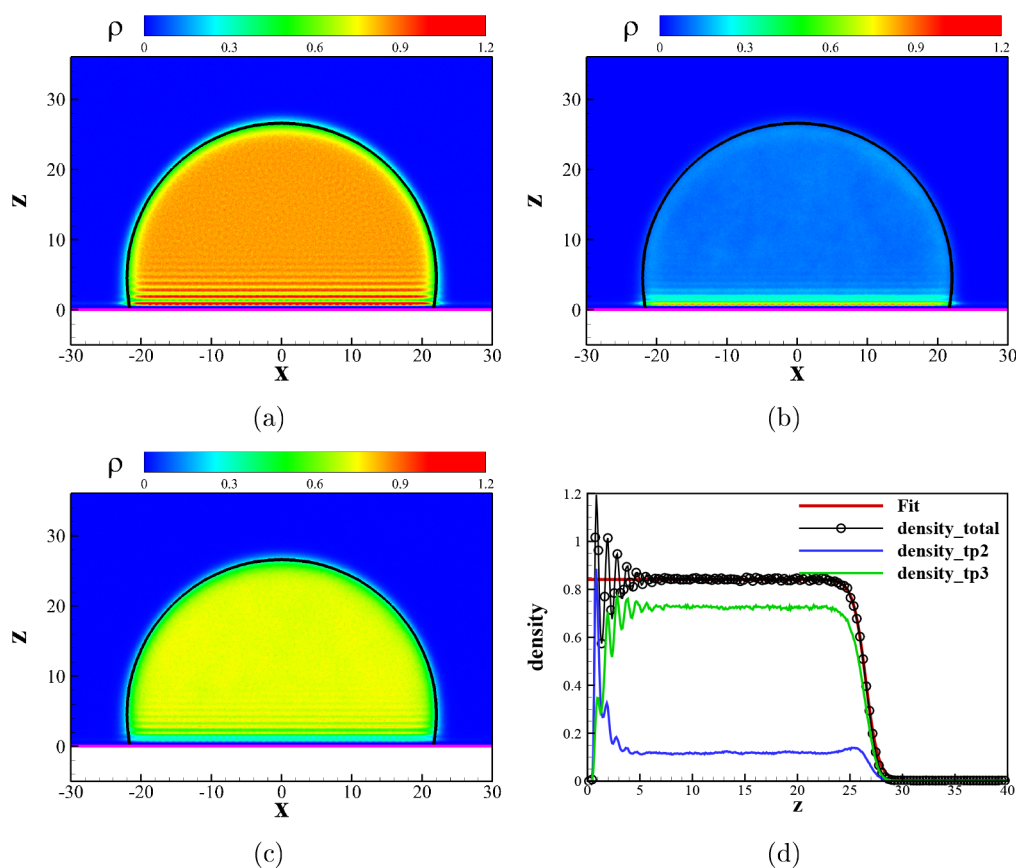
Figure 3. Density contour of the binary droplet (a), hydrophilic component (b), and hydrophobic component (c). In each panel, the pink solid line represents the surface of solid substrate, and the black arc represents the liquid−vapor interface. (d) Number density along $x = 0$ which passes through the center of the binary droplet, as a function of z. The black, blue, and green lines represent the curves of the binary droplet (labeled as "total"), the hydrophilic (labeled as "tp2"), and hydrophobic components (labeled as "tp3"), respectively. The red solid line represents the fitting curve of the binary droplet. The temperature of the system is $T = 0.67$. The other key parameters of this case are $\varepsilon_{23} = 0.9$ and $\varphi = 0.2$.

because there is no obvious stratification. When $\varepsilon_{23} > 0.9$, the two components in the droplet are well-mixed and instantaneous shapes all look like Figure 1(b).

The coordination number C_{ij} as the average number of j-type particles surrounding i-type particles within a radius of $2\sigma_{22}$ is used to quantify the mixing degree. When C_{23} and C_{22} are close, type-2 and type-3 particles almost have equal opportunity to surround a type-2 particle. Hence, the two particles are highly soluble in each other. When C_{23} is significantly different from C_{22}, the two particles are not well-mixed. Coordination number C_{ij} as a function of time for different ε_{23} is shown in Figure 1(a) when the system temperature is $T = 0.67$ and $\varphi = 0.5$. For the stable system, C_{23}/C_{22} as a function of ε_{23} is shown in Figure 2(b). When $0.8 \leq \varepsilon_{23} < 0.9$, C_{23}/C_{22} increased sharply from 0.18 to 0.90. When $0.9 \leq \varepsilon_{23} < 1.15$, C_{23}/C_{22} increased slowly from 0.90 to 1.15. Hence, a strong mutual interaction (a larger ε_{23}) with respect to the self-interaction (ε_{22}) leads to a well-mixed state. Here we are more interested in the well-mixed state. Hence, in the following discussion, ε_{23} is chosen to be 0.9, 1.0, and 1.1. They represent the typical cases in which the mutual interaction ε_{23} is smaller than, equal to, and larger than the self-interaction between type-2 and type-2 or type-3 and type-3 ($\varepsilon_{33} = \varepsilon_{22}$).

■ RESULTS AND DISCUSSION

Density in Equilibrium State. First, we have to verify the correctness of the simulation. At the equilibrium state, the binary droplet is surrounded by the vapor phase and the droplet volume becomes constant. Here we suppose the binary droplet is a cap of a perfect cylinder, although the instantaneous shape shown in Figure 1(b) may slightly

different from a cap of cylinder due to statistical fluctuations. Here, a case for $\varepsilon_{23} = 0.9$ and $\varphi = 0.2$ is taken as an example to explore the density distribution in the equilibrium state ($T = 0.67$).

Density contours for the binary droplet, hydrophilic and hydrophobic components are shown in Figure 3(a−c), respectively. In each panel, the pink solid line represents the surface of the solid substrate, and the black arc represents the liquid−vapor interface, which is the contour of $(\rho(r) - \rho_g)/(\rho_l - \rho_g) = 0.5$, where $\rho_l = 0.841$, $\rho_g = 0.002$ are liquid and vapor number densities, respectively. It can be seen that the number density contours are stratified near the substrate. In the bulk phase, the number density is uniform, but at the liquid−vapor interface, it decreases sharply in Figure 3(a) and Figure 3(c).

Number density along $x = 0$ as a function of z is shown in Figure 3(d). The black, blue, and green lines represent the number densities of a binary droplet (labeled as "total"), hydrophilic (labeled as "tp2"), and hydrophobic components (labeled as "tp3"), respectively. It can be seen that there are large fluctuations near the liquid−solid interface due to the strong interaction between the solid and liquid atoms. The density becomes much smoother when $z > 5.0$. Near the wall, the peak value of the number density of type-2 particles decreases with the increase of z, while for type-3 particles, the situation is reversed. Hence, although the number fraction of type-2 particles is small ($\varphi = 0.2$), the first density peak value
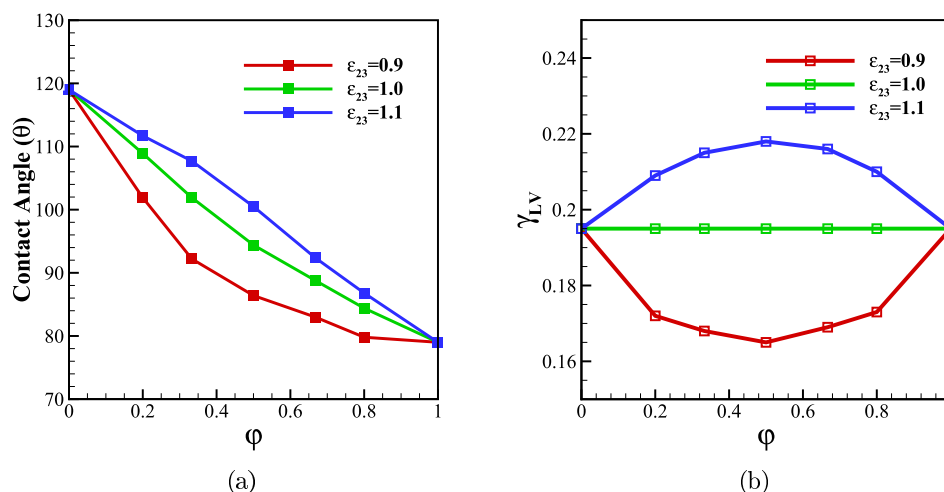
Figure 4. (a) The equilibrium contact angle (θ) as a function of φ for different ε_{23}. (b) The surface tension (γ_{LV}) as a function of φ for different ε_{23}. The temperature of the system is $T = 0.67$.
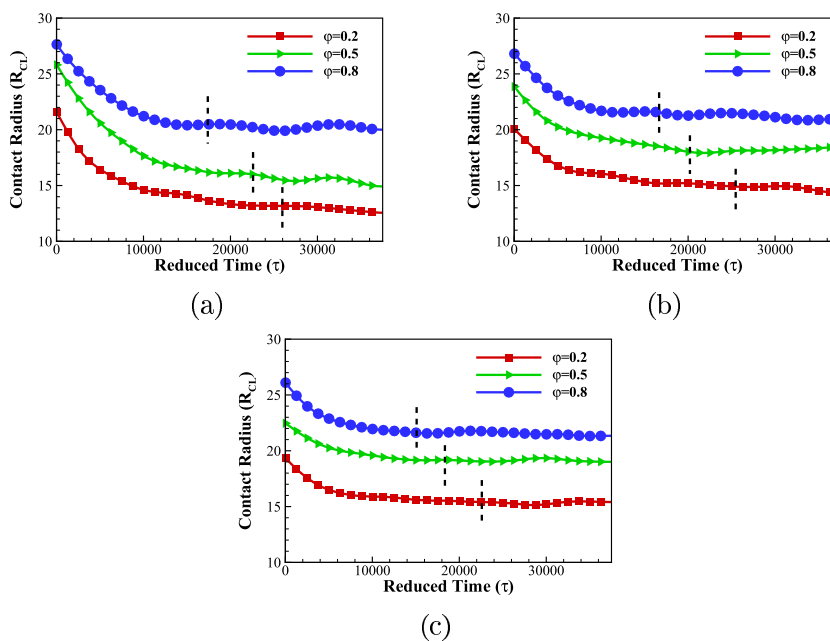

Figure 5. Contact radius (R_{CL}) as a function of time for different φ. (a) $\varepsilon_{23} = 0.9$, (b) $\varepsilon_{23} = 1.0$, (c) $\varepsilon_{23} = 1.1$. The short vertical black dashed line in each curve represents the moment after which the evaporation reaches an equilibrium state.

of type-2 particles near the wall is much larger than that of type-3 particles because type-2 particles are hydrophilic.

As a whole, the number density of the binary droplet as a function of z can be fitted by a hyperbolic tangent curve

$$\rho = \frac{1}{2}(\rho_l + \rho_g) - \frac{1}{2}(\rho_l - \rho_g)\tanh\left[\frac{2(z - z_0)}{d_s}\right] \quad (2)$$

$z_0 = 26.5$ is the height of the droplet and $d_s = 2.5$ is the liquid–vapor interface thickness. It is seen that excluding the points of $z < 5.0$, the fitted curve agrees well with the simulation data. This result is consistent with the result of pure droplets,[49] so our simulation is valid.

Equilibrium Contact Angle and Surface Tension. Evaporation of single-component droplets on a homogeneous surface has been studied by predecessors using MD simulation. They found that the main factor affecting evaporation of the single-component droplets is hydrophobicity, which is

characterized by contact angle. However, for binary droplets, besides contact angle, surface tension may also affect droplet evaporation, which has never been studied. Here we will study the effects of contact angle and surface tension on evaporation behavior.

When the liquid–vapor interface is captured accurately, the contact angle can be obtained. The equilibrium contact angle (θ) as a function of φ for different ε_{23} when $T = 0.67$ is shown in Figure 4(a). It is seen that θ decreases with φ. It can be understood as follows. When φ is large, there are more hydrophilic particles in the binary droplet. Therefore the droplet becomes more hydrophilic. In the meanwhile, at a specific φ, the larger ε_{23}, the more hydrophobic the droplet becomes. Because when ε_{23} increases, the concentration of hydrophilic particles (type-2 particles) near the TPCL will decrease. The surface tension (γ_{LV}) as a function of φ at $T = 0.67$ is shown in Figure 4(b) The surface tension can be calculated by integrating the difference between normal
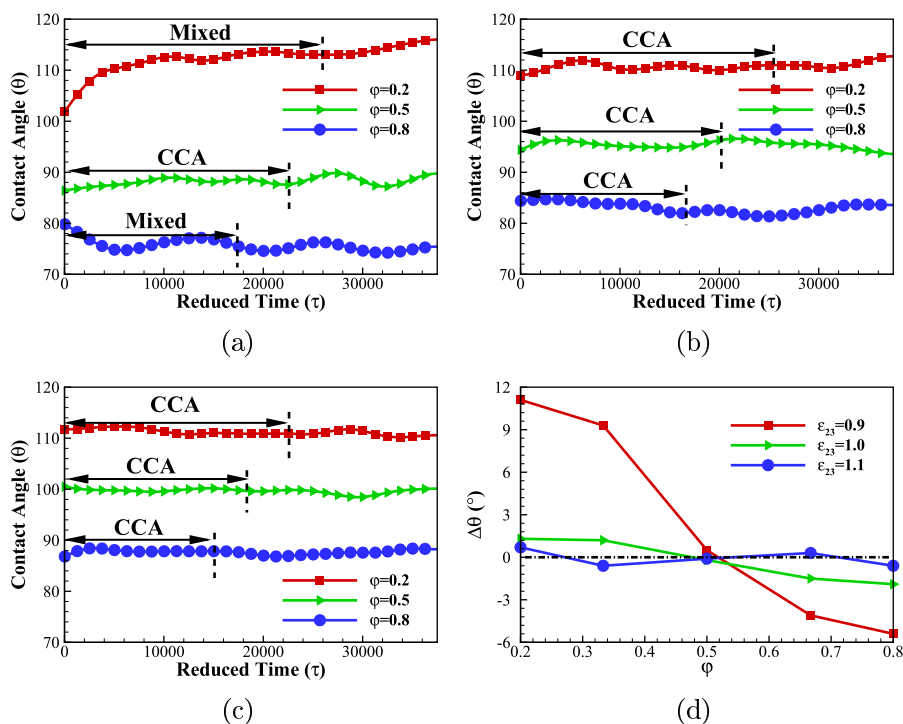
Figure 6. Contact angle (θ) as a function of time for different φ. (a) $\varepsilon_{23} = 0.9$, (b) $\varepsilon_{23} = 1.0$, (c) $\varepsilon_{23} = 1.1$. The short vertical black dashed line in each curve represents the moment after which the evaporation reaches an equilibrium state. (d) The change of contact angle ($\Delta\theta = \theta_{T=0.83} - \theta_{T=0.67}$) as a function of φ, where $\theta_{T=0.83}$, $\theta_{T=0.67}$ represent the equilibrium contact angle at $T = 0.83$ and 0.67, respectively. The horizontal black dotted line denotes $\Delta\theta = 0°$.

($p_n(z)$) and tangential ($p_t(z)$) components of the pressure tensor across the liquid−vapor interface,[56,57]

$$\gamma_{LV} = \int (p_n(z) - p_t(z))\, \mathrm{d}z \tag{3}$$

where z represents the thickness of the liquid−vapor interface (see Figure 3(a) and Figure 3(d)). For $\varepsilon_{23} = 1.0$, γ_{LV} does not change with φ, because type-2 and type-3 particles are exactly the same particles under the circumstance. As we know, liquid−vapor surface tension results from the greater attraction of liquid molecules to each other (due to cohesion) than to the molecules in the vapor (due to adhesion). When the liquid particle interaction in the interface vicinity of a droplet is weak, the liquid−vapor surface tension γ_{LV} should be small. It is seen that for $\varepsilon_{23} = 0.9$, γ_{LV} decreases first and then increases with the increase of φ, and it reaches the minimum at $\varphi = 0.5$. It is noticed that at $\varphi = 0.5$, the attraction of liquid molecules to each other is weakest among all cases with different φ for $\varepsilon_{23} = 0.9$ because the mutual interaction parameter ε_{23} is smaller than the self-interaction parameters ε_{22} and ε_{33} ($\varepsilon_{33} = \varepsilon_{22}$). Hence γ_{LV} would be smallest at $\varphi = 0.5$ for $\varepsilon_{23} = 0.9$. For the cases of $\varepsilon_{23} = 1.1$, the situation is reversed and γ_{LV} reaches the maximum at $\varphi = 0.5$. This is because the mutual interaction parameter ε_{23} is larger than the self-interaction parameters ε_{22} and ε_{33} ($\varepsilon_{33} = \varepsilon_{22}$).

Evaporation Pattern. To quantify the evolution of the droplet during the evaporation, the contact angle (θ) and contact radius (R_{CL}) of binary droplets during evaporation were calculated. Figure 5(a−c) show R_{CL} as a function of time when $\varepsilon_{23} = 0.9$, 1.0 and 1.1, respectively. It is seen that all curves first decrease fast and then converge to a plateau. Each evaporation curve can be divided into two parts by the short vertical black dashed lines at $t = t'$. The left part of each curve

($t < t'$) represents the initial or the first stage where the binary droplet absorbs heat from the wall and then evaporate. The right part ($t > t'$) of each curve represents the equilibrium state at $T = 0.83$ (the second stage). In the second state, the evaporation and condensation reach equilibrium. It is also seen for a specific ε_{23}, e.g., $\varepsilon_{23} = 0.9$ (Figure 5(a)) the larger the φ, the larger the contact radius at the equilibrium state. A possible reason is that the droplet is more hydrophilic at a larger φ. Therefore we would discuss the evolution of contact angle during the evaporation.

Figure 6(a−c) show the contact angle as a function of time for $\varepsilon_{23} = 0.9$, 1.0, and 1.1, respectively. Previous studies have assumed that the evaporation mode of a single component droplet at ideal interfaces (flat, completely smooth, and chemically homogeneous) is CCA mode, and there is no pinning phenomenon. For binary droplets, our simulation results also support this hypothesis when $\varepsilon_{23} \geq 1.0$ (see Figure 6(b) and Figure 6(c)). When $\varepsilon_{23} = 1.0$ and 1.1, θ of each curve approximately remains constant in the first stage with a decreasing R_{CL}. This is the CCA mode. When $\varepsilon_{23} = 0.9$, there are more evaporation modes for different φ. From Figure 6(a) and Figure 5(a), it is seen that in the case of $\varphi = 0.5$, θ is constant and R_{CL} decreases. The evaporation mode is the CCA mode. In the cases of $\varphi = 0.2$ and $\varphi = 0.8$, neither θ nor R_{CL} are constant in the first stage. Their evaporation mode is the mixed mode. It is also noticed that in all of our simulations, no CCR mode was observed in the first stage.

It is also seen that in the second stage, both θ and R_{CL} are almost constant with small fluctuations. Two possible reasons may contribute to the fluctuations. One reason is that the instantaneous shape of a binary droplet is not a perfect cylinder. The other reason is that an error would be raised if the statistics are insufficient.
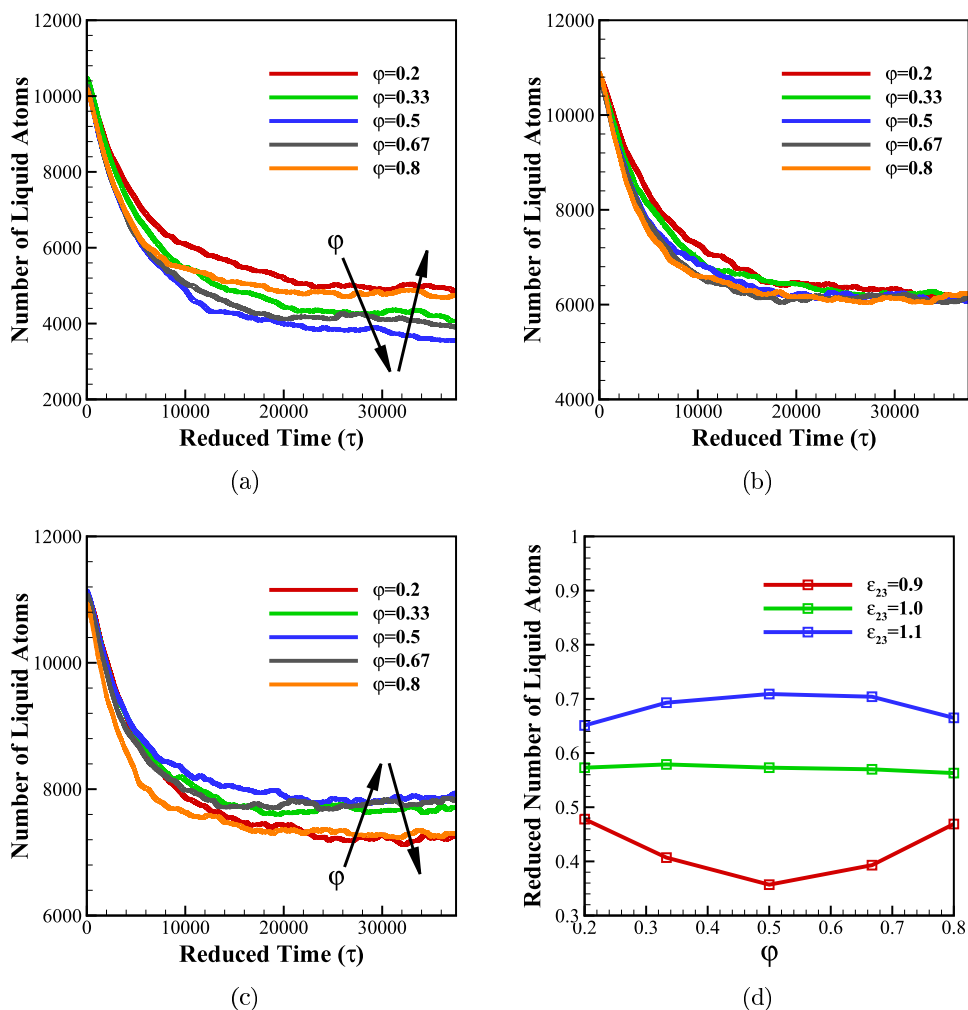
Figure 7. (a−c) The number of binary liquid atoms (N) as a function of time for different φ. (a) $\varepsilon_{23} = 0.9$, (b) $\varepsilon_{23} = 1.0$, (c) $\varepsilon_{23} = 1.1$. (d) The reduced number of liquid atoms ($\overline{N}$) as a function of φ for different ε_{23} at $T = 0.83$. For comparison, all parameters have been normalized by the number of liquid atoms at $T = 0.67$.

In order to reduce the statistical error, we calculated the change of contact angle before and after droplet evaporation. The change of contact angle ($\Delta\theta = \theta_{T=0.83} - \theta_{T=0.67}$) as a function of φ is shown in Figure 6(d). $\theta_{T=0.83}$, $\theta_{T=0.67}$ represent the equilibrium contact angle at $T = 0.83$ and 0.67, respectively. The contact angle here is the corresponding time-averaged contact angle. It is seen that $|\Delta\theta| < 2°$ when $\varepsilon_{23} \geq 1.0$. Therefore, the evaporation mode is CCA mode if the fluctuation of θ is ignored. When $\varepsilon_{23} = 0.9$, the evaporation mode of the case of $\varphi = 0.5$ is the CCA. However, the cases with $\varphi < 0.5$, $\Delta\theta$ is significantly larger than 0°. The situation is reversed for the cases with $\varphi > 0.5$. In summary, a larger ε_{23}, or $\varphi \approx 0.5$ would lead to the CCA evaporation mode. When ε_{23} is small, the mixed mode may appear. In addition, the pinning phenomenon was not observed in our simulations.

Binary Droplet Size. In this section, the size evolution of the binary droplet would be discussed. To analyze the droplet size, the cluster analysis was performed.[49] In the analysis, two atoms were considered to be part of the same cluster if the distance between them was smaller than $1.5\sigma_{22}$. The number of binary liquid atoms as a function of time for different φ is shown in Figures 7(a) to 7(c). In all cases of $\varepsilon_{23} = 0.9$ (see Figure 7(a)), when the substrate's temperature suddenly increases, the binary droplet size decreases quickly. Later

because the vapor pressure becomes more and more saturated, the system reaches an equilibrium state at $T = 0.83$ and the number of droplet atoms becomes constant in each case. It is seen that approximately the larger the φ, the faster the droplet evaporates. The possible reason is that when φ is large, the droplet is more hydrophilic and the contacting area would be larger. In this way, the heat transfer from the wall to the binary droplet would be more efficient.

It is also seen that the number of droplet atoms at the equilibrium state is different in the cases. When φ changes from 0.2 to 0.8, the number of equilibrium binary droplets decreases first and then increases, and it reaches a minimum value at $\varphi = 0.5$. The variation trend is consistent with that of γ_{LV} for $\varepsilon_{23} = 0.9$ (see Figure 4(b)). In the case of $\varphi = 0.5$, since γ_{LV} becomes the smallest, the number of saturated vapor particles would be the largest. As the total number of liquid−vapor particles is constant, the number of binary droplet atoms would be the smallest.

For $\varepsilon_{23} = 1.0$ and 1.1, the variation trend of the droplet size looks similar to that of $\varepsilon_{23} = 0.9$. For $\varepsilon_{23} = 1.0$, the number of binary droplet particles in the final equilibrium state is approximately identical in all cases. This can be attributed to the identical γ_{LV} in all cases. For $\varepsilon_{23} = 1.1$, the number of binary droplets at the equilibrium state increases with φ at first.
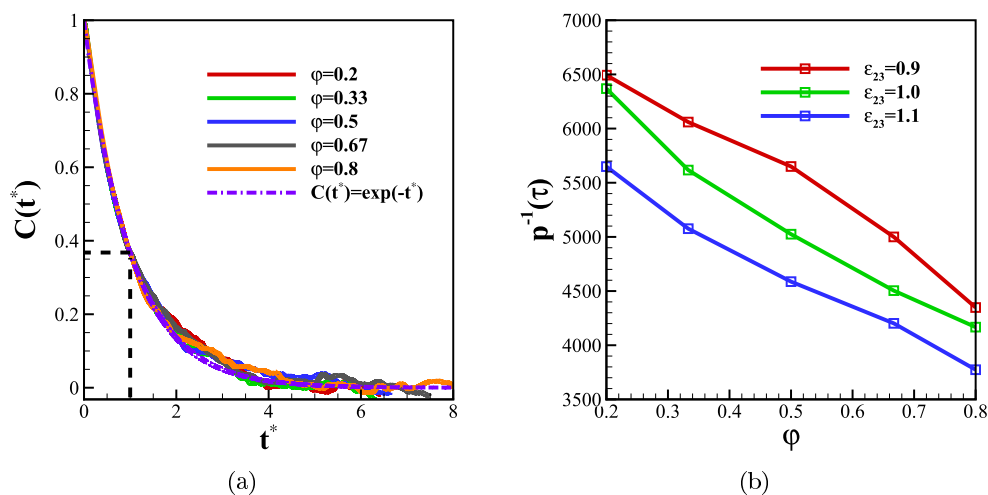
Figure 8. (a) The normalized number of liquid atoms as a function of the normalized time for different φ when $\varepsilon_{23} = 0.9$. The purple dotted-line represents the theoretical solution. The vertical black dashed line denotes $t^* = 1$, and the horizontal black dashed line denotes $C(t^*) = 1/e$. (b) The relaxation time (p^{-1}) as a function of φ for different ε_{23}.
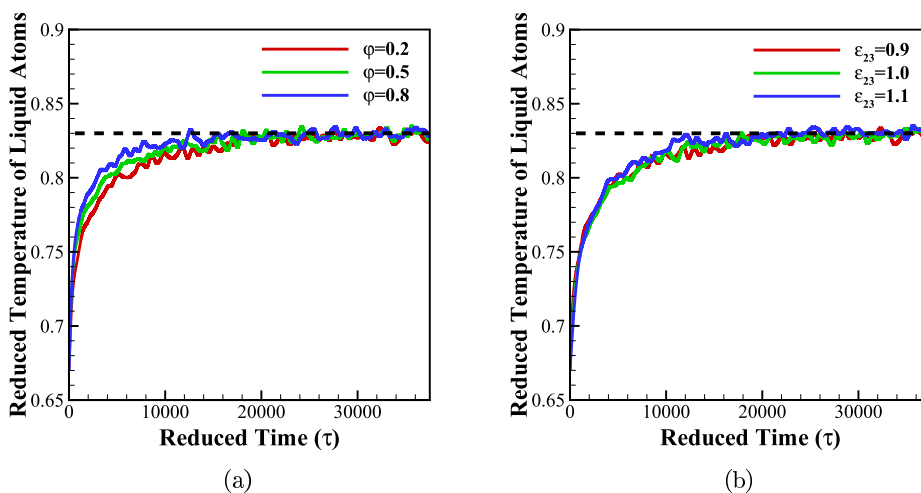

Figure 9. (a) The average temperature of binary droplets as a function of time for different φ when $\varepsilon_{23} = 0.9$. (b) The average temperature of binary droplets as a function of time for different ε_{23} when $\varphi = 0.2$.

It reaches the maximum at $\varphi = 0.5$ and then decreases with φ. This is also attributed to the variation trend of γ_{LV} for $\varepsilon_{23} = 1.1$ in Figure 4(b).

The reduced number of liquid atoms $\bar{N}$ as a function of φ for different ε_{23} at $T = 0.83$ is shown in Figure 7(d). $\bar{N}$ is normalized by the initial number of liquid atoms at $T = 0.67$. It is seen that at a specific φ, $\bar{N}$ increases with ε_{23}. For example, at $\varphi = 0.5$, $\bar{N}$ in the case of $\varepsilon_{23} = 1.1$ is 0.71, which is twice as much as that in $\varepsilon_{23} = 09$. The variation trend of $\bar{N}$ looks similar to that of γ_{LV} in Figure 4(b). Therefore, the number of binary droplet particles strongly depends on γ_{LV}. It is noted that the initial number of binary droplets in cases with different ε_{23} at $T = 0.63$ may be slightly different but the difference is negligible. For example, the initial number of binary droplets is 10 300, 10 700, and 11 000 in the cases with $\varepsilon_{23} = 0.9$, 1.0, and 1.1, respectively.

According to our previous study,[54] during the evaporation, the number of droplets N as a function of time (t) can be written as

$$N(t) = N(\infty) + [N(0) - N(\infty)] \times e^{-pt} \quad (4)$$

where $N(0)$ and $N(\infty)$ are the number of the binary droplets at $t = 0$ and $t = \infty$, respectively. $N(\infty)$ is the time-average value after $t = 27\,500\tau$. p^{-1} is the relaxation time and can be obtained through solving $C(t) = (N(t) - N(\infty))/(N(0) - N(\infty)) = 1/e$, where $C(t)$ is the normalized number of binary droplets. If the evaporation time is normalized by the relaxation time (p^{-1}), i.e., $t^* = t/(p^{-1})$, then eq 4 can be rewritten as

$$C(t^*) = e^{-t^*} \quad (5)$$

We take $\varepsilon_{23} = 0.9$ as an example. $C(t^*)$ as a function of t^* for different φ when $\varepsilon_{23} = 0.9$ is shown in Figure 8(a). We can see that our simulation results are in good agreement with the theoretical curve, especially when $t^* \leq 1.0$.

The relaxation time (p^{-1}) as a function of φ for different ε_{23} is shown in Figure 8(b). The relaxation time can be used to quantify the evaporation speed of binary droplet evaporation. The smaller the relaxation time, the faster the binary droplet evaporates. First, we can see that p^{-1} becomes smaller and smaller with the increase of φ, which is consistent with the
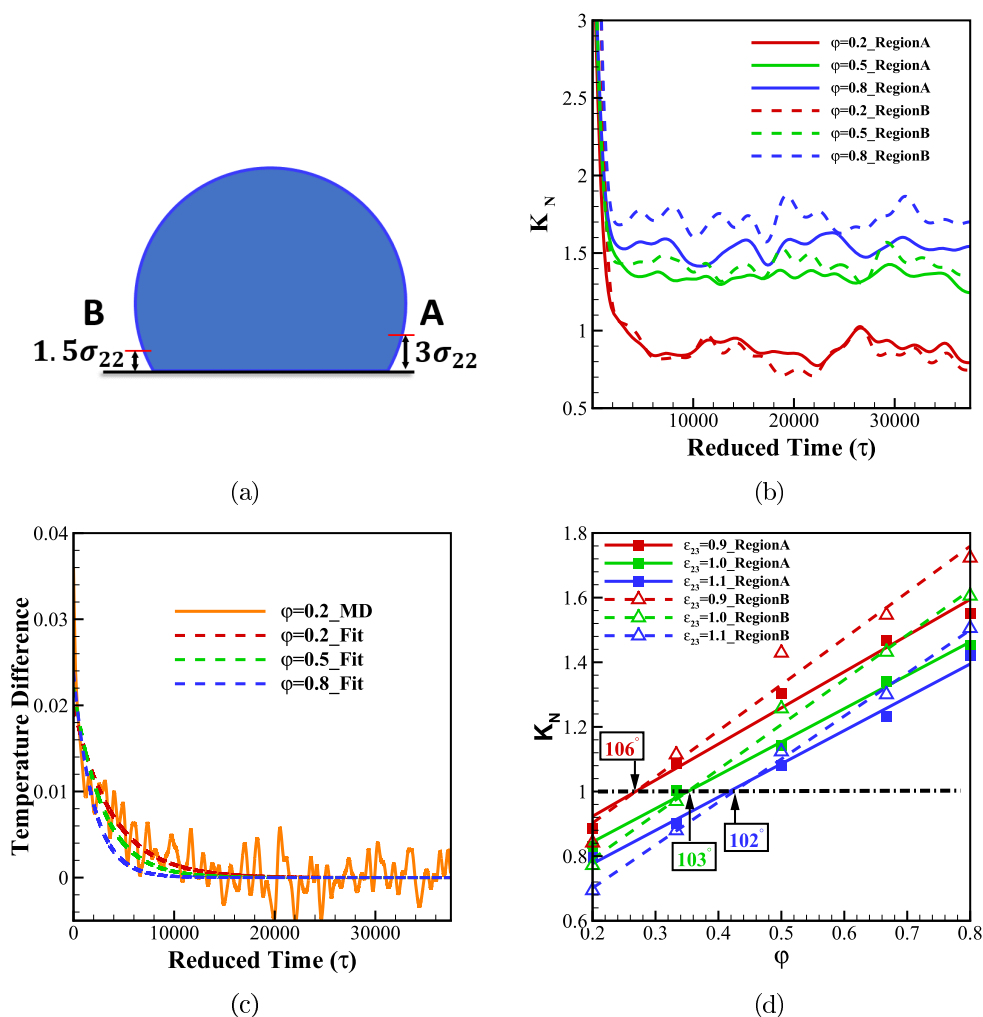
Figure 10. (a) Definition of the regions of the three-phase contact line. Regions A and B have thicknesses of $3\sigma_{22}$ and $1.5\sigma_{22}$, respectively. (b) The evaporation ratio of local mass flux (K_N) for different φ when $\varepsilon_{23} = 0.9$. The solid and dashed lines represent the K_N obtained from Region A and B, respectively. (c) Reduced temperature difference ($\Delta T = T_{TPCL} - T_{droplet}$) as a function of time for cases of $\varepsilon_{23} = 0.9$. T_{TPCL}, $T_{droplet}$ are the average temperature of the TPCL Region A and that of the rest of the droplet. The solid and dashed lines represent the simulation and the fitting data, respectively. (d) The evaporation ratio of local mass flux (K_N) as a function of φ for different ε_{23}. The solid and dashed lines represent the K_{N_A} and K_{N_B}, respectively. The black dotted line denotes $K_N = 1$.

impression in Figures 7(a) to 7(c). Second, we can see that for a fixed φ, p^{-1} decreases with the increase of ε_{23}.

The relaxation time p^{-1} may depend on two aspects: heat transfer between liquid and solid and heat transfer between liquid and liquid. When the substrate temperature suddenly increases, first the heat transfers from the substrate to the droplet near the wall. Then the heat is transferred inside the droplet until it reaches the liquid−vapor interface. Finally, the liquid particles with higher kinetic energy evaporate from the liquid−vapor interfacial region. The heat transfer between liquid and solid can be described by the average temperature of binary droplets. The higher the droplet temperature, the faster the heat transfer between the liquid−solid interface.

The average temperature of binary droplets as a function of time for different φ when $\varepsilon_{23} = 0.9$ is shown in Figure 9(a). It can be seen that the larger the φ, the faster the drop temperature will rise. This phenomenon is attributed to the fact that in the case with a large φ, the droplet is more hydrophilic and the contact area would be large, which results in a higher efficiency of heat transfer from the solid wall to the droplet. So p^{-1} becomes smaller with the increase of φ. The

average temperature of binary droplets as a function of time for different ε_{23} when $\varphi = 0.2$ is shown in Figure 9(b). It can be seen that for cases with different ε_{23}, the discrepancy is negligible. Therefore the heat transfer efficiency between the liquid−solid interfaces does not depend on ε_{23}. However, with the increase of ε_{23}, the heat transfer efficiency between the liquid interior is improved. That would promote the evaporation. Hence, p^{-1} also decreases with the increase of ε_{23}.

Local Mass Flux. In the above section, we mainly discussed the overall heat and mass transfer during the evaporation, but the distribution of heat and mass transfer at the liquid−vapor interface may be uneven. It has been found that most heat and mass transfer occurs near the three-phase contact line (TPCL) during the evaporation.[58] In order to investigate whether the point is valid at nanometer scale, we calculated the evaporation ratio of local mass flux. The evaporation ratio of local mass flux (K_N) can be calculated using the following formula:

$$K_N = \frac{N_L/S_L}{N_T/S_T} \tag{6}$$

where N_L and N_T represent the particle number evaporated from the TPCL area in unit time and that from the whole liquid−vapor interface in unit time, respectively. S_L and S_T represent the area of TPCL and the whole liquid−vapor interface, respectively. $K_N > 1$ and $K_N < 1$ represent situations where the particle mass flux in the TPCL area is promoted and suppressed, respectively.

It is noted that how to define the TPCL area is an open question. To be more general, here two different TPCL regions were defined. One region has a thickness of $3\sigma_{22}$, i.e., the threshold distance between liquid atoms and the substrate is $3\sigma_{22}$. The other has a thickness of $1.5\sigma_{22}$, see Figure 10(a). They are referred to as Region A and Region B, respectively in the following description. K_N calculated from Region A and B are referred to as K_{N_A} and K_{N_B}, respectively. Here we take the case of $\varepsilon_{23} = 0.9$ as an example. The evaporation ratio of local mass flux (K_N) for different φ is shown in Figure 10(b). It is seen that K_N curves decrease first and then reach a plateau with small oscillation. The decrease of K_N arises from the reduction in the temperature difference between the TPCL region and the rest of the binary droplet. At the beginning of the simulation, when the temperature of the substrate is suddenly increased, the liquid atoms closest to the substrate first absorb heat and gain a higher temperature than the atoms in the rest of the droplet. Reduced temperature difference ($\Delta T = T_{\text{TPCL}} - T_{\text{droplet}}$) as a function of time is shown in Figure 10(c). T_{TPCL} and T_{droplet} are average temperature of the TPCL Region A and that of the rest of the droplet, respectively. It can be seen that the temperature differences are over 0.02 at the beginning of the evaporation. The evaporation occurring in the TPCL region is therefore faster than that elsewhere. Then we have $K_N > 1$ in these simulations. Due to the continuous heat transfer from the substrate to the droplet, ΔT decreases and gradually becomes zero. Thus, the relative importance of evaporation at the TPCL decreases gradually. When $\Delta T \approx 0$, K_N converges to a constant value.

From Figure 10(b), it can also be seen that when $\varphi = 0.5$ and 0.8, the converged K_{N_B} is significantly larger than K_{N_A}. They are all larger than unity, i.e., $K_N > 1$. It seems that, when the binary droplet is hydrophilic, the local mass flux is promoted in the TPCL. Besides, the closer the defined TPCL region is to the wall, the greater the promotion. When $\varphi = 0.2$, the converged $K_N < 1$. It seems that when the binary droplet is hydrophobic, the local mass flux is inhibited in the TPCL. When $\varepsilon_{23} = 1.0$ and 1.1, the results of K_N are similar to those of $\varepsilon_{23} = 0.9$.

For the local mass transfer, we are particularly concerned with the boundary of contact angle (θ_c) where the evaporation of particles near the TPCL transits from the promoted state to the inhibited state ($K_N = 1$). According to the traditional theoretical analysis, the boundary is $\theta_c = 90°$.[59,60] In addition, the mass flux of a hydrophobic droplet decreases from the droplet apex to the TPCL, while the mass flux of a hydrophilic droplet increases from the droplet apex to the TPCL. Zhang et al.[49] studied the local mass flux during the evaporation of a single component droplet on a homogeneous surface by MD. They claimed that the distribution of the mass flux at the hydrophobic droplet's liquid−vapor interface is uniform and $K_N > 1$. Hence, the MD simulation result may be different from theoretical analysis. Here this issue is also investigated in detail.

The evaporation ratio of local mass flux (K_N) as a function of φ for different ε_{23} is shown in Figure 10(d). K_N is calculated by

the average value when $t > 27\,500$. First we can seen that in the cases of $\varepsilon_{23} = 0.9$, 1.0 and 1.1, we have $K_N = 1$ at $\varphi = 0.27$, 0.35, and 0.42, respectively. The corresponding θ_c is 106°, 103°, and 102°, respectively. The result is different from the theoretical result. Second, we can also see that for K_{N_A} or K_{N_B}, when φ is fixed, K_N decreases with the increases of ε_{23}. These conclusions may be related to the adsorption layer near the solid wall, which will be discussed in the following.

To analyze the adsorption layer near the solid wall, we show a typical instantaneous snapshot of the binary droplet evaporation in Figure 11. The yellow ellipses in Figure 11
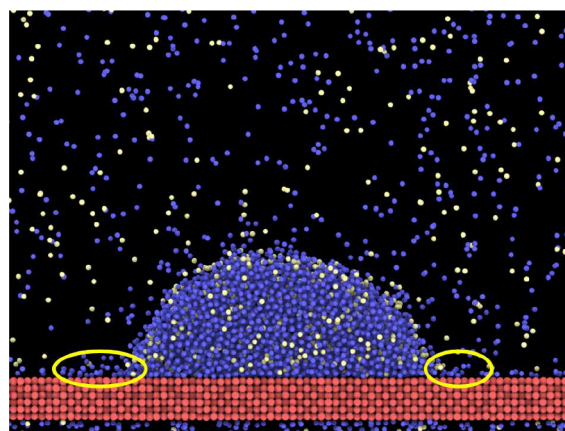

Figure 11. Typical instantaneous snapshot of the binary droplet evaporation when $\varepsilon_{23} = 0.9$, $\varphi = 0.8$. The yellow ellipses represent the adsorption layer near the TPCL.

show that there is an adsorption layer near the TPCL when the binary droplet is hydrophilic. When the binary droplet evaporates, the adsorption layer also evaporates. Therefore, the particles evaporating from the adsorption layer may be counted as those evaporating from the TPCL region, which makes K_N larger. The higher the density of the adsorbed layer, the greater the promotion of K_N.

The number density of particles in the adsorption layer (ρ_a) as a function of z near the solid wall for cases of $\varepsilon_{23} = 0.9$ is shown in Figure 12(a). It can be seen that there is a high density adsorption layer near the wall ($z = 0.9\sigma_{22}$). The larger the φ, the higher the ρ_a. This is because the hydrophilic particles in the vapor phase are easy to be adsorbed on the solid surface. It is also seen that even for the hydrophobic binary droplets ($\varphi = 0.2$), the density of the adsorption layer is about 0.03, which can not be neglected. From the above analysis, it can be concluded that the promotion of K_N decreases with the increase of θ. It is noticed that even for the hydrophobic droplets, K_N will also have a small increase due to the existence of adsorption layer. In this way, due to the uneven promotion of K_N, θ_c will shift to the hydrophobic direction when the droplets evaporate at the nanoscale (see schematic diagram Figure 12(c)). In Figure 12(c), the solid and dashed lines denote the theoretical and simulation results, respectively. And the larger the ρ_a, the larger the θ_c will be.

The number density of particles in the adsorption layer as a function of z near the solid wall for various ε_{23} when $\varphi = 0.2$ is shown in Figure 12(b). It can be seen that with the increase of ε_{23}, the number density of the adsorption layer decreases. This means that the stronger the interaction between type-2 and type-3 particles, the less K_N will be promoted. To some extent,
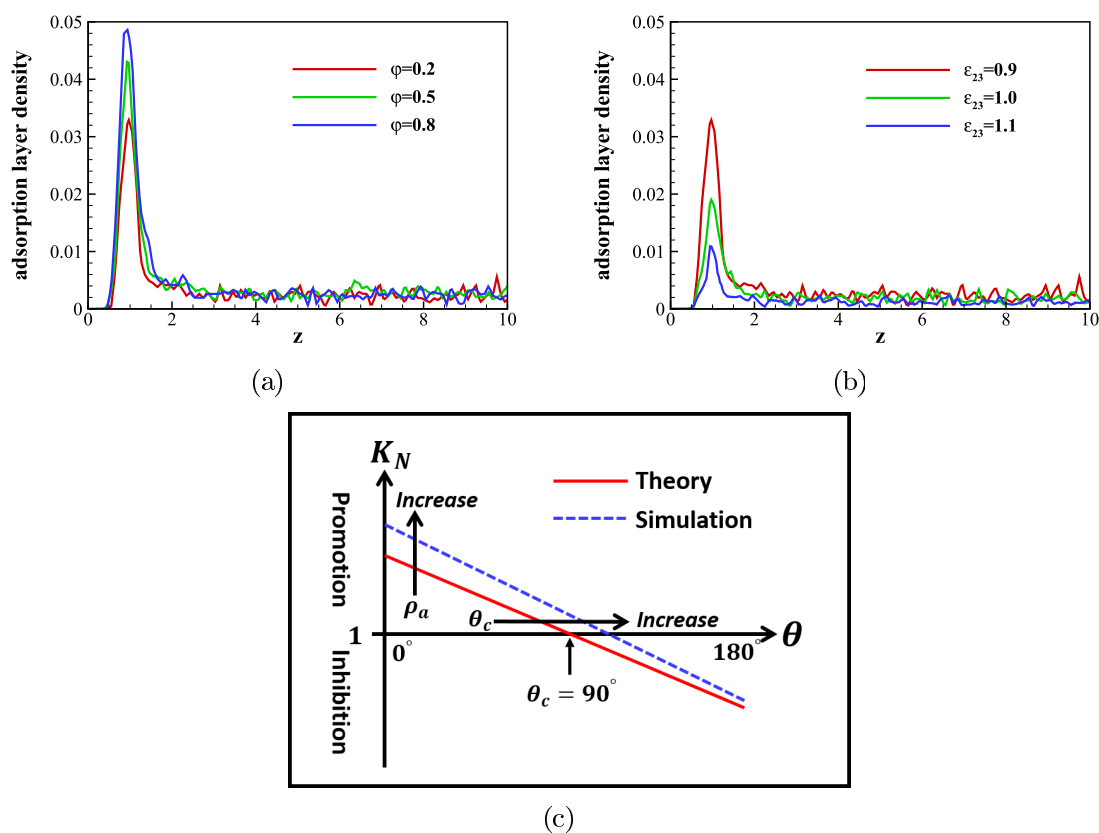
Figure 12. (a) The number density of particles in the adsorption layer (ρ_a) as a function of z for different φ when ε_{23} = 0.9. (b) The number density of particles in the adsorption layer (ρ_a) as a function of z for different ε_{23} when φ = 0.2. (c) Schematic diagram of K_N changing with θ. The solid and dashed lines denote the theoretical and simulation results, respectively.

it also shows that the larger the ε_{23}, the smaller the θ_c. This is consistent with the first conclusion.

SUMMARY AND CONCLUSIONS

The evaporation of a cylindrical binary nanodroplet consisting of Lennard–Jones particles on homogeneous surfaces was studied by molecular dynamics simulations. The binary droplets contain a hydrophilic component (type-2 particles) and a hydrophobic component (type-3 particles), which lead to different contact angles. As far as we know, this is the first time MD methods are used to study binary droplet evaporation. To study the effect of surface tension and substrate wettability on the evaporation, simulations with different liquid–liquid interactions ε_{23} and number fraction of hydrophilic particles φ were performed.

First, we investigated how the equilibrium contact angle θ and surface tension γ_{LV} change with parameters φ and ε_{23} at T = 0.67. A large φ would result in a small θ since the hydrophilic component becomes dominant. At a specific φ, θ may increase with ε_{23}. The variation of γ_{LV} is more complicated. For ε_{23} = 1.0, γ_{LV} does not change with φ. For ε_{23} = 0.9, γ_{LV} decreases first and then increases with φ. For the cases of ε_{23} = 1.1, the situation is reversed.

Second, the evolution of contact angle and contact radius for the binary droplet during evaporation was analyzed. It is observed that when the interaction between type-2 and type-3 particles is not repulsion, ($\varepsilon_{23} \geq 1.0$), its evaporation mode is CCA mode. When the interaction between type-2 and type-3 particles is repulsion ($\varepsilon_{23} < 1.0$), the situation is a little bit complicated. When φ = 0.5, the evaporation mode is also CCA

mode. When $\varphi \neq 0.5$, it is the mixed mode. In addition, there is no pinning phenomenon in all cases due to the homogeneous surface.

Third, the variation of binary droplet number with time during evaporation was examined. The relaxation time (p^{-1}) is used to characterize the speed of binary droplet evaporation. Generally speaking, increasing φ and ε_{23} would promote the heat transfer efficiency between liquid and solid and that inside the droplet, respectively. That results in a smaller p^{-1}.

Finally, the evaporation ratio of local mass flux was explored. We found that the critical contact angle (θ_c) where the local mass flux transits from the promoted state to the suppressed state near the TPCL is about 102° to 106°. It is different from the theory one (90°). The discrepancy between the simulated and theoretical results increases as ε_{23} decreases. The discrepancy is attributed to the existence of the adsorption layer near the TPCL.

AUTHOR INFORMATION

Corresponding Author

Haibo Huang − *Department of Modern Mechanics, University of Science and Technology of China, Hefei, Anhui 230026, China;* ⓞ orcid.org/0000-0002-1308-9900; Email: huanghb@ ustc.edu.cn

Authors

Jia-Jian Zhang − *Department of Modern Mechanics, University of Science and Technology of China, Hefei, Anhui 230026, China*

Xi-Yun Lu − *Department of Modern Mechanics, University of Science and Technology of China, Hefei, Anhui 230026, China*

■ REFERENCES

(1) Park, J.; Moon, J. Control of colloidal particle deposit patterns within picoliter droplets ejected by ink-jet printing. *Langmuir* **2006**, *22*, 3506−3513.

(2) Creran, B.; Li, X.; Duncan, B.; Kim, C. S.; Moyano, D. F.; Rotello, V. M. Detection of bacteria using inkjet-printed enzymatic test strips. *ACS Appl. Mater. Interfaces* **2014**, *6*, 19525−19530.

(3) Jing, J.; Reed, J.; Huang, J.; Hu, X.; Clarke, V.; Edington, J.; Housman, D.; Anantharaman, T. S.; Huff, E. J.; Mishra, B.; et al. Automated high resolution optical mapping using arrayed, fluid-fixed DNA molecules. *Proc. Natl. Acad. Sci. U. S. A.* **1998**, *95*, 8046−8051.

(4) Hsieh, C.-C.; Li, L.; Larson, R. G. Modeling hydrodynamic interaction in Brownian dynamics: simulations of extensional flows of dilute solutions of DNA and polystyrene. *J. Non-Newtonian Fluid Mech.* **2003**, *113*, 147−191.

(5) Xia, D.; Brueck, S. A facile approach to directed assembly of patterns of nanoparticles using interference lithography and spin coating. *Nano Lett.* **2004**, *4*, 1295−1299.

(6) Bigioni, T. P.; Lin, X.-M.; Nguyen, T. T.; Corwin, E. I.; Witten, T. A.; Jaeger, H. M. Kinetically driven self assembly of highly ordered nanoparticle monolayers. *Nat. Mater.* **2006**, *5*, 265.

(7) Deegan, R. D.; Bakajin, O.; Dupont, T. F.; Huber, G.; Nagel, S. R.; Witten, T. A. Capillary flow as the cause of ring stains from dried liquid drops. *Nature* **1997**, *389*, 827.

(8) Deegan, R. D.; Bakajin, O.; Dupont, T. F.; Huber, G.; Nagel, S. R.; Witten, T. A. Contact line deposits in an evaporating drop. *Phys. Rev. E: Stat. Phys., Plasmas, Fluids, Relat. Interdiscip. Top.* **2000**, *62*, 756.

(9) Birdi, K.; Vu, D.; Winter, A. A study of the evaporation rates of small water drops placed on a solid surface. *J. Phys. Chem.* **1989**, *93*, 3702−3703.

(10) Erbil, H. Y.; McHale, G.; Newton, M. Drop evaporation on solid surfaces: constant contact angle mode. *Langmuir* **2002**, *18*, 2636−2641.

(11) Hu, H.; Larson, R. G. Evaporation of a sessile droplet on a substrate. *J. Phys. Chem. B* **2002**, *106*, 1334−1344.

(12) Xu, W.; Leeladhar, R.; Kang, Y. T.; Choi, C.-H. Evaporation kinetics of sessile water droplets on micropillared superhydrophobic surfaces. *Langmuir* **2013**, *29*, 6032−6041.

(13) Rowan, S. M.; Newton, M.; McHale, G. Evaporation of microdroplets and the wetting of solid surfaces. *J. Phys. Chem.* **1995**, *99*, 13268−13271.

(14) Ristenpart, W.; Kim, P.; Domingues, C.; Wan, J.; Stone, H. Influence of substrate conductivity on circulation reversal in evaporating drops. *Phys. Rev. Lett.* **2007**, *99*, 234502.

(15) Hu, H.; Larson, R. G. Analysis of the microfluid flow in an evaporating sessile droplet. *Langmuir* **2005**, *21*, 3963−3971.

(16) Zhang, J.; Leroy, F.; Müller-Plathe, F. Influence of contact-line curvature on the evaporation of nanodroplets from solid substrates. *Phys. Rev. Lett.* **2014**, *113*, 046101.

(17) Orejon, D.; Sefiane, K.; Shanahan, M. E. Stick−slip of evaporating droplets: substrate hydrophobicity and nanoparticle concentration. *Langmuir* **2011**, *27*, 12834−12843.

(18) Moffat, J. R.; Sefiane, K.; Shanahan, M. E. Effect of TiO2 nanoparticles on contact line stick- slip behavior of volatile drops. *J. Phys. Chem. B* **2009**, *113*, 8860−8866.

(19) Chen, X.; Ma, R.; Li, J.; Hao, C.; Guo, W.; Luk, B. L.; Li, S. C.; Yao, S.; Wang, Z. Evaporation of droplets on superhydrophobic surfaces: Surface roughness and small droplet size effects. *Phys. Rev. Lett.* **2012**, *109*, 116101.

(20) Li, Q.; Zhou, P.; Yan, H. Pinning−depinning mechanism of the contact line during evaporation on chemically patterned surfaces: a lattice Boltzmann study. *Langmuir* **2016**, *32*, 9389−9396.

(21) Xu, W.; Choi, C.-H. Effects of surface topography and colloid particles on the evaporation kinetics of sessile droplets on super-hydrophobic surfaces. *J. Heat Transfer* **2012**, *134*, 051022.

(22) Maxwell, J. C. *The Scientific Papers of James Clerk Maxwell*; University Press, 1890; Vol. 2.

(23) Kusumaatmaja, H.; Yeomans, J. Modeling contact angle hysteresis on chemically patterned and superhydrophobic surfaces. *Langmuir* **2007**, *23*, 6019−6032.

(24) Agarwal, A. K. Biofuels (alcohols and biodiesel) applications as fuels for internal combustion engines. *Prog. Energy Combust. Sci.* **2007**, *33*, 233−271.

(25) Tchakalova, V.; Zemb, T.; Benczédi, D. Evaporation triggered self-assembly in aqueous fragrance−ethanol mixtures and its impact on fragrance performance. *Colloids Surf., A* **2014**, *460*, 414−421.

(26) Lu, Y.; Fan, H.; Stump, A.; Ward, T. L.; Rieker, T.; Brinker, C. J. Aerosol-assisted self-assembly of mesostructured spherical nano-particles. *Nature* **1999**, *398*, 223.

(27) Brinker, C. J.; Lu, Y.; Sellinger, A.; Fan, H. Evaporation-induced self-assembly: nanostructures made easy. *Adv. Mater.* **1999**, *11*, 579−585.

(28) Carreón, Y. J.; González-Gutiérrez, J.; Pérez-Camacho, M.; Mercado-Uribe, H. Patterns produced by dried droplets of protein binary mixtures suspended in water. *Colloids Surf., B* **2018**, *161*, 103−110.

(29) Kim, H.; Boulogne, F.; Um, E.; Jacobi, I.; Button, E.; Stone, H. A. Controlled uniform coating from the interplay of Marangoni flows and surface-adsorbed macromolecules. *Phys. Rev. Lett.* **2016**, *116*, 124501.

(30) Sefiane, K.; Tadrist, L.; Douglas, M. Experimental study of evaporating water−ethanol mixture sessile drop: influence of concentration. *Int. J. Heat Mass Transfer* **2003**, *46*, 4527−4534.

(31) Sefiane, K. On the Dynamic Capillary Effects in the Wetting and evaporation process of Binary Droplets. *Fluid Dynam. Mater. Process.* **2005**, *1*, 267−276.

(32) Rusdi, M.; Moroi, Y.; Nakahara, H.; Shibata, O. Evaporation from Water- Ethylene Glycol Liquid Mixture. *Langmuir* **2005**, *21*, 7308−7310.

(33) Cheng, A. K.; Soolaman, D. M.; Yu, H.-Z. Evaporation of Microdroplets of Ethanol- Water Mixtures on Gold Surfaces Modified with Self-Assembled Monolayers. *J. Phys. Chem. B* **2006**, *110*, 11267−11271.

(34) Sefiane, K.; David, S.; Shanahan, M. E. Wetting and evaporation of binary mixture drops. *J. Phys. Chem. B* **2008**, *112*, 11317−11323.

(35) Innocenzi, P.; Malfatti, L.; Costacurta, S.; Kidchob, T.; Piccinini, M.; Marcelli, A. Evaporation of ethanol and ethanol-water mixtures studied by time-resolved infrared spectroscopy. *J. Phys. Chem. A* **2008**, *112*, 6512−6516.

(36) Liu, C.; Bonaccurso, E.; Butt, H.-J. Evaporation of sessile water/ethanol drops in a controlled environment. *Phys. Chem. Chem. Phys.* **2008**, *10*, 7150−7157.

(37) Wang, Z.; Peng, X.-F.; Mujumdar, A. S.; Su, A.; Lee, D.-J. Evaporation of ethanol-water mixture drop on horizontal substrate. *Drying Technol.* **2008**, *26*, 806−810.

(38) Shi, L.; Shen, P.; Zhang, D.; Lin, Q.; Jiang, Q. Wetting and evaporation behaviors of water−ethanol sessile drops on PTFE surfaces. *Surf. Interface Anal.* **2009**, *41*, 951−955.

(39) Raj, M. D.; Mandal, D. K.; Navaneethakrishnan, S.; Bakshi, S. Measurement of the surface concentration (liquid) of an evaporating multicomponent droplet using pendant droplet method. *Exp. Fluids* **2010**, *48*, 715−719.

(40) Hamamoto, Y.; Christy, J. R.; Sefiane, K. The flow characteristics of an evaporating ethanol water mixture droplet on a glass substrate. *J. Therm. Sci. Technol.* **2012**, *7*, 425−436.

(41) Erbil, H. Y. Control of stain geometry by drop evaporation of surfactant containing dispersions. *Adv. Colloid Interface Sci.* **2015**, *222*, 275−290.

(42) Chen, P.; Toubal, M.; Carlier, J.; Harmand, S.; Nongaillard, B.; Bigerelle, M. Evaporation of binary sessile drops: infrared and acoustic methods to track alcohol concentration at the interface and on the surface. *Langmuir* **2016**, *32*, 9836−9845.

(43) Feng, H.; Chong, K. S.-L.; Ong, K.-S.; Duan, F. Octagon to square wetting area transition of water−ethanol droplets on a micropyramid substrate by increasing ethanol concentration. *Langmuir* **2017**, *33*, 1147−1154.

(44) Diddens, C.; Kuerten, J. G.; Van der Geld, C.; Wijshoff, H. Modeling the evaporation of sessile multi-component droplets. *J. Colloid Interface Sci.* **2017**, *487*, 426−436.

(45) Tan, H.; Diddens, C.; Lv, P.; Kuerten, J.; Zhang, X.; Lohse, D. Evaporation-triggered microdroplet nucleation and the four life phases of an evaporating Ouzo drop. *Proc. Natl. Acad. Sci. U. S. A.* **2016**, *113*, 8642−8647.

(46) Diddens, C. Detailed finite element method modeling of evaporating multi-component droplets. *J. Comput. Phys.* **2017**, *340*, 670−687.

(47) Wang, F.-C.; Wu, H.-A. Pinning and depinning mechanism of the contact line during evaporation of nano-droplets sessile on textured surfaces. *Soft Matter* **2013**, *9*, 5703−5709.

(48) Zhang, J.; Müller-Plathe, F.; Leroy, F. Pinning of the contact line during evaporation on heterogeneous surfaces: slowdown or temporary immobilization? Insights from a nanoscale study. *Langmuir* **2015**, *31*, 7544−7552.

(49) Zhang, J.; Leroy, F.; Müller-Plathe, F. Evaporation of nanodroplets on heated substrates: a molecular dynamics simulation study. *Langmuir* **2013**, *29*, 9770−9782.

(50) Wan, R.; Wang, C.; Lei, X.; Zhou, G.; Fang, H. Enhancement of water evaporation on solid surfaces with nanoscale hydrophobic-hydrophilic patterns. *Phys. Rev. Lett.* **2015**, *115*, 195901.

(51) Wang, S.; Tu, Y.; Wan, R.; Fang, H. Evaporation of tiny water aggregation on solid surfaces with different wetting properties. *J. Phys. Chem. B* **2012**, *116*, 13863−13867.

(52) Xie, C.; Liu, G.; Wang, M. Evaporation flux distribution of drops on a hydrophilic or hydrophobic flat surface by molecular simulations. *Langmuir* **2016**, *32*, 8255−8264.

(53) Yu, J.-J.; Tang, R.; Li, Y.-R.; Zhang, L.; Wu, C.-M. Molecular Dynamics Simulation of Heat Transport through Solid−Liquid Interface during Argon Droplet Evaporation on Heated Substrates. *Langmuir* **2019**, *35*, 2164−2171.

(54) Zhang, J.; Huang, H.; Lu, X.-Y. Pinning−Depinning Mechanism of the Contact Line during Evaporation of Nanodroplets on Heated Heterogeneous Surfaces: A Molecular Dynamics Simulation. *Langmuir* **2019**, *35*, 6356−6366.

(55) Plimpton, S. Fast parallel algorithms for short-range molecular dynamics. *J. Comput. Phys.* **1995**, *117*, 1−19.

(56) Kirkwood, J. G.; Buff, F. P. The Statistical Mechanical Theory of Surface Tension. *J. Chem. Phys.* **1949**, *17*, 338−343.

(57) Marchand, A.; Weijs, J. H.; Snoeijer, J. H.; Andreotti, B. Why is surface tension a force parallel to the interface? *Am. J. Phys.* **2011**, *79*, 999−1008.

(58) Stephan, P.; Busse, C. Analysis of the heat transfer coefficient of grooved heat pipe evaporator walls. *Int. J. Heat Mass Transfer* **1992**, *35*, 383−391.

(59) Nguyen, T. A.; Nguyen, A. V.; Hampton, M. A.; Xu, Z. P.; Huang, L.; Rudolph, V. Theoretical and experimental analysis of droplet evaporation on solid surfaces. *Chem. Eng. Sci.* **2012**, *69*, 522−529.

(60) Kadhim, M. A.; Kapur, N.; Summers, J. L.; Thompson, H. Experimental and Theoretical Investigation of Droplet Evaporation on Heated Hydrophilic and Hydrophobic Surfaces. *Langmuir* **2019**, *35*, 6256−6266.